THE ASTROPHYSICAL JOURNAL LETTERS, 922:L9 (10pp), 2021 November 20 https://doi.org/10.3847/2041-8213/ac2c62

Physical Characterization of Main-belt Comet (248370) 2005 QN_{173}

Henry H. Hsieh[1,2], Colin O. Chandler[3], Larry Denneau[4], Alan Fitzsimmons[5], Nicolas Erasmus[6], Michael S. P. Kelley[7], Matthew M. Knight[7,8], Tim A. Lister[9], Jana Pittichová[10], Scott S. Sheppard[11], Audrey Thirouin[12], Chadwick A. Trujillo[3], Helen Usher[13], Edward Gomez[14], Joey Chatelain[9], Sarah Greenstreet[15,16], Tony Angel[17], Richard Miles[18], Paul Roche[19], and Ben Wooding[20]

[1] Planetary Science Institute, 1700 East Fort Lowell Road, Suite 106, Tucson, AZ 85719, USA; hhsieh@psi.edu
[2] Institute of Astronomy and Astrophysics, Academia Sinica, P.O. Box 23-141, Taipei 10617, Taiwan
[3] Department of Astronomy and Planetary Science, Northern Arizona University, Flagstaff, AZ 86011, USA
[4] Institute for Astronomy, University of Hawaii, 2680 Woodlawn Drive, Honolulu, HI 96822, USA
[5] Astrophysics Research Centre, School of Physics and Astronomy, Queen's University Belfast, Belfast BT7 1NN, UK
[6] South African Astronomical Observatory, Cape Town, 7925, South Africa
[7] Department of Astronomy, University of Maryland, 1113 Physical Sciences Complex, Building 415, College Park, MD 20742, USA
[8] Department of Physics, U.S. Naval Academy, 572C Holloway Road, Annapolis, MD 21402, USA
[9] Las Cumbres Observatory, 6740 Cortona Drive, Suite 102, Goleta, CA 93117, USA
[10] Jet Propulsion Laboratory, California Institute of Technology, 4800 Oak Grove Drive, Pasadena, CA 91109, USA
[11] Earth and Planets Laboratory, Carnegie Institution for Science, 5241 Broad Branch Road NW, Washington, DC 20015, USA
[12] Lowell Observatory, 1400 West Mars Hill Road, Flagstaff, AZ 86001, USA
[13] The Open University, Walton Hall, Milton Keynes, MK7 6AA, UK
[14] Las Cumbres Observatory, School of Physics and Astronomy, Cardiff University, Queens Buildings, The Parade, Cardiff CF24 3AA, UK
[15] Asteroid Institute, 20 Sunnyside Avenue, Suite 427, Mill Valley, CA 94941, USA
[16] Department of Astronomy and the DIRAC Institute, University of Washington, 3910 15th Ave NE, Seattle, WA 98195, USA
[17] Harlingten Observatory, Observatorio Sierra Contraviesa, Cortijo El Cerezo, Torvizcon E-18430, Granada, Spain
[18] British Astronomical Association, UK
[19] Faulkes Telescope Project, School of Physics and Astronomy, Cardiff University, Cardiff, CF24 3AA, UK
[20] St Mary's Catholic Primary School, Llangewydd Road, Bridgend, Wales, CF31 4JW, UK
Received 2021 August 25; revised 2021 September 28; accepted 2021 September 29; published 2021 November 17

Abstract

We report results from new and archival observations of the newly discovered active asteroid (248370) 2005 QN_{173} (also now designated Comet 433P), which has been determined to be a likely main-belt comet based on a subsequent discovery that it is recurrently active near perihelion. From archival data analysis, we estimate g'-, r'-, i'-, and z'-band absolute magnitudes for the nucleus of $H_g = 16.62 \pm 0.13$, $H_r = 16.12 \pm 0.10$, $H_i = 16.05 \pm 0.11$, and $H_z = 15.93 \pm 0.08$, corresponding to nucleus colors of $g' - r' = 0.50 \pm 0.16$, $r' - i' = 0.07 \pm 0.15$, and $i' - z' = 0.12 \pm 0.14$; an equivalent V-band absolute magnitude of $H_V = 16.32 \pm 0.08$; and a nucleus radius of $r_n = 1.6 \pm 0.2$ km (using a V-band albedo of $p_V = 0.054 \pm 0.012$). Meanwhile, we find mean near-nucleus coma colors when 248370 is active of $g' - r' = 0.47 \pm 0.03$, $r' - i' = 0.10 \pm 0.04$, and $i' - z' = 0.05 \pm 0.05$ and similar mean dust tail colors, suggesting that no significant gas coma is present. We find approximate ratios between the scattering cross sections of near-nucleus dust (within 5000 km of the nucleus) and the nucleus of $A_d/A_n = 0.7 \pm 0.3$ on 2016 July 22 and $1.8 < A_d/A_n < 2.9$ in 2021 July and August. During the 2021 observation period, the coma declined in intrinsic brightness by ~0.35 mag (or ~25%) in 37 days, while the surface brightness of the dust tail remained effectively constant over the same period. Constraints derived from the sunward extent of the coma and width of the tail as measured perpendicular to the orbit plane suggest that the terminal velocities of ejected dust grains are extremely slow (~1 m s^{-1} for 1 μm particles), suggesting that the observed dust emission may be aided by rapid rotation of the nucleus lowering the effective escape velocity.

Unified Astronomy Thesaurus concepts: Main-belt comets (2131); Comets (280); Comae (2015); Comet nuclei (2160); Comet tails (274); Main belt asteroids (2036); Asteroids (72); Small Solar System bodies (1469)

1. Introduction

Asteroid (248370) 2005 QN_{173} (hereafter 248370; also recently designated Comet 433P) was discovered to be active on UT 2021 July 7 in data comprising 120 s of total exposure time (Figure 1(e)) obtained by the Asteroid Terrestrial-impact Last Alert System (ATLAS; Tonry et al. 2018a) survey telescope (Fitzsimmons et al. 2021). On that date, the object was at a heliocentric distance of $r_h = 2.391$ au and true anomaly of $\nu = 16\overset{\circ}{.}0$, having most recently reached perihelion on UT 2021 May 14. As reported in the discovery announcement, 248370 exhibited a thin, straight dust tail $7\overset{\prime}{.}6$ in length at a position angle of 245° east of north in confirmation observations obtained by Lowell Observatory's 4.3 m Lowell Discovery Telescope (LDT). Zwicky Transient Facility observations show the presence of the tail as early as UT 2021 June 11 (Kelley et al. 2021).

As of 2021 August 1, 248370 had a semimajor axis of $a = 3.067$ au, eccentricity of $e = 0.226$, and inclination of $i = 0\overset{\circ}{.}067$, according to the JPL Small-Body Database,[21] placing it unambiguously in the outer main asteroid belt. Its active nature and asteroidal orbit places it among the class of objects known as active asteroids, which exhibit comet-like mass loss yet have dynamically asteroidal orbits (Jewitt et al. 2015). Active asteroids include main-belt comets (MBCs; Hsieh & Jewitt 2006), for which sublimation of volatile ice is the most likely activity driver, and disrupted asteroids, for

[21] https://ssd.jpl.nasa.gov/sbdb.cgi

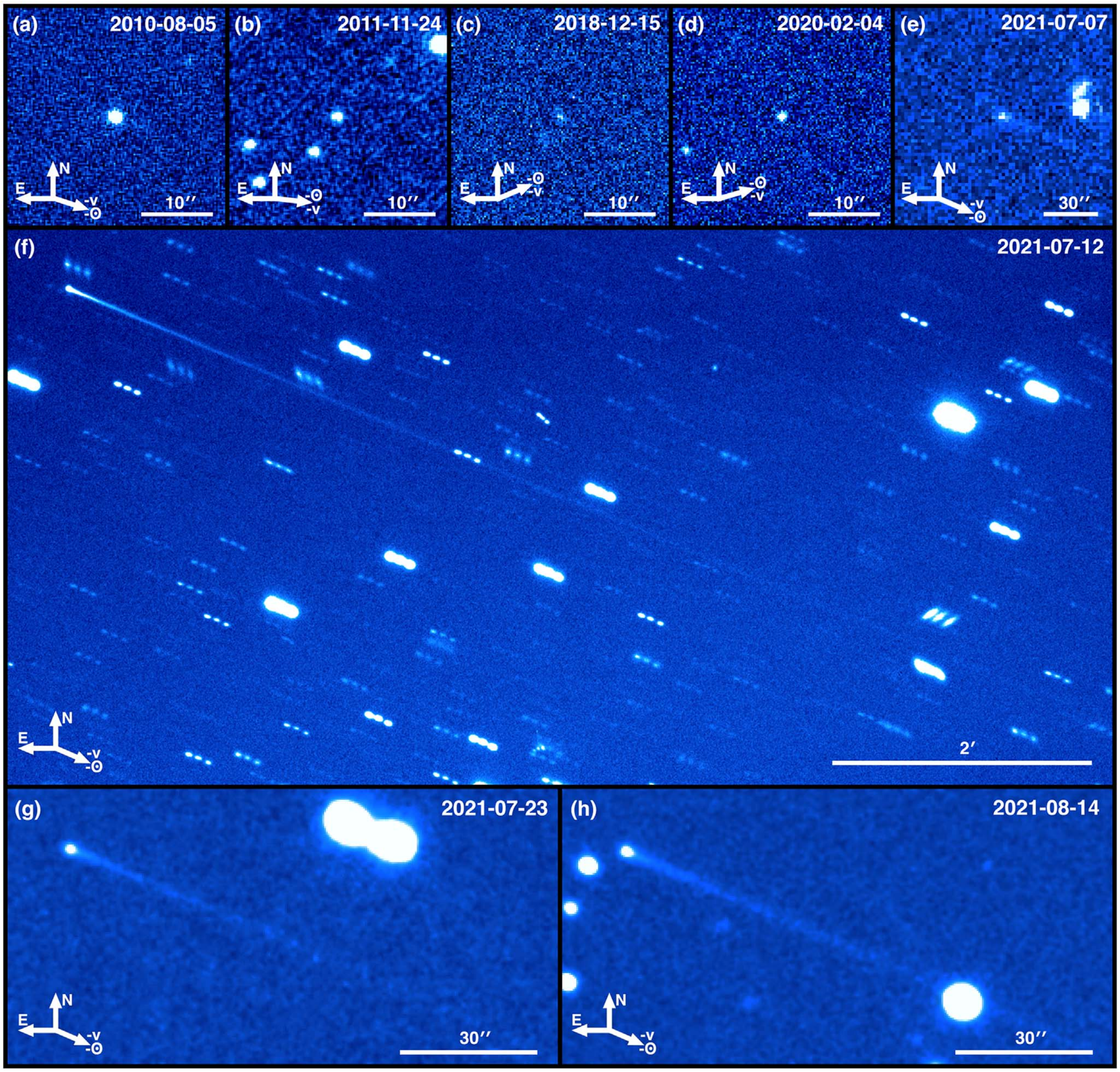

Figure 1. Single or composite images of 248370 for the dates indicated in each panel (see Tables 1 and 2 for observation details). All images are in the r' band except for panel (e), which was obtained using the ATLAS survey's "cyan" filter (bandpass from 420 to 650 nm). Scale bars indicate the size of each panel. North (N), east (E), the antisolar direction ($-\odot$), and the negative heliocentric velocity direction ($-v$) are indicated in each panel. The object is located at the center of panels (a)–(e), while in panels (f)–(h), the object's nucleus is located in the upper left corner with the tail extending down and to the right, where the latter set of images have been Gaussian smoothed to enhance the visibility of low surface brightness features.

which activity is due to other processes, such as impacts or rotational destabilization (e.g., Hsieh et al. 2012).

Asteroid 248370 has previously been measured to have a diameter of 3.6 ± 0.2 km and visible geometric albedo of 0.054 ± 0.012 using $H_V = 16.00$ for the v-band absolute magnitude and $G = 0.15$ (Mainzer et al. 2019). As of 2021 July, there were no published rotational light-curve data available for the object in the Asteroid Lightcurve Photometry Database[22] or the NASA Planetary Data System[23] (PDS). Similarly, no taxonomic classification for 248370 is available in current PDS catalogs.

Following the discovery of 248370's activity in 2021, Chandler et al. (2021a) reported the discovery of activity in archival data from the Dark Energy Camera (DECam; Flaugher et al. 2015) on the 4 m Victor M. Blanco Telescope (hereafter Blanco) at Cerro Tololo Interamerican Observatory (CTIO) obtained on UT 2016 July 22, when the object was at a true anomaly of $\nu = 56\overset{\circ}{.}5$, having then most recently passed perihelion on UT 2016 January 3. This discovery of two separate active apparitions of 248370, both near perihelion, is considered a strong indication that sublimation is responsible

[22] https://minplanobs.org/alcdef/index.php
[23] https://pds.nasa.gov/

for the observed activity (e.g., Hsieh et al. 2012; Chandler et al., 2021b).

2. Observations

New observations of 248370 were obtained on several nights between UT 2021 July 8 and UT 2021 August 14 with LDT (Levine et al. 2012), Palomar Observatory's 5 m Hale Telescope (hereafter Palomar), the 2 m Faulkes Telescope North (FTN), and the Las Cumbres Observatory (LCOGT) 1 m telescopes (Brown et al. 2013) at CTIO and the South African Astronomical Observatory. Details of these observations are shown in Table 1, where, for reference, ATLAS discovery observation details are also shown, although no further analysis is conducted of those observations due to the use of a nonstandardized filter. Observations were obtained using the LDT's Large Monolithic Imager (Bida et al. 2014), Palomar's Wafer-Scale camera for Prime (Nikzad et al. 2017) wide-field prime focus camera, FTN's Multicolor Simultaneous Camera for studying Atmospheres of Transiting exoplanets (MuSCAT3; Narita et al. 2020), and the LCOGT Sinistro cameras. All observations were obtained using Sloan g'-, r'-, i'-, or z'-band filters and nonsidereal tracking to follow the target's motion.

Multifilter FTN data were obtained using the simultaneous g'-, r'-, i'-, and z'-band imaging capability of MuSCAT3. Multifilter Palomar observations were obtained by interspersing filters (i.e., using repeating $r'g'r'i'r'$ or $r'i'g'r'$ sequences) to enable the use of interpolation to approximate simultaneous multifilter imaging for color computation (i.e., compensating for possible rotational variability in the nucleus brightness between our actual observations in different filters).

Bias subtraction, flat-field correction, and cosmic-ray removal were performed for LDT and Palomar data using the Python 3 code utilizing the `ccdproc` package in Astropy (Astropy Collaboration et al. 2018) and the `L.A.Cosmic` code[24] (van Dokkum 2001; van Dokkum et al. 2012). The FTN and LCOGT 1 m data were processed using standard LCOGT pipeline software (McCully et al. 2018).

We also used the Canadian Astronomy Data Centre's Solar System Object Image Search tool[25] (Gwyn et al. 2012) and the NASA PDS Small Bodies Node's Comet Asteroid Telescopic Catalog Hub tool[26] to identify archival Sloan g'-, r'-, i'-, and z'-band observations of 248370 from 2004 to 2020 (Table 2) from the 1.8 m Panoramic Survey Telescope and Rapid Response System (Pan-STARRS1; hereafter PS1) survey telescope (Chambers et al. 2016; Flewelling et al. 2020), MegaCam (Boulade et al. 2003) on the 3.6 m Canada–France–Hawaii Telescope (CFHT), the 1.35 m SkyMapper survey telescope (Wolf et al. 2018), and Blanco. For the purposes of our analysis, PS1 g_{P1}, r_{P1}, i_{P1}, and z_{P1} filters are considered functionally equivalent to their Sloan counterparts (see Tonry et al. 2012). All archival data were pipeline processed by their respective facilities.

The object was identified in archival images either from its nonsidereal motion when more than one image was available on a particular night or from comparison with reference images obtained on other nights when the object was not in the field of view.

3. Results and Analysis

3.1. Data Analysis

Except for data from 2016 July 22, 248370 had a starlike surface brightness profile in all archival images and exhibited no other visible indications of activity. Meanwhile, in all 2021 observations, the object exhibited a long, straight dust tail oriented along the coincident antisolar and negative heliocentric velocity vector directions as projected on the sky. In our best composite image from UT 2021 July 12, the tail was seen extending $\sim 9'$ from the nucleus (Figure 1(f)), corresponding to a physical extent of $\sim$720,000 km at the geocentric distance of the comet. A minimal coma was present in all images, with FWHM measurements of the nucleus's surface brightness profile measured in the direction perpendicular to the dust tail nearly identical to FWHM measurements, θ_s, of field star profiles (listed in Table 1) measured in the direction perpendicular to their trailing due to nonsidereal tracking. We did, however, find the half-width at half-maximum (HWHM) of the object's profile measured along the sunward direction directly opposite the dust tail to be $\sim$10% larger than stellar HWHM values, suggesting the presence of a dust coma, which will be discussed in Section 3.3.3.

To maximize signal-to-noise ratios (S/Ns) for sets of observations where more than one image was obtained in the same filter in a night, we constructed composite images by shifting and aligning individual images in each filter on the object's photocenter using linear interpolation and adding them together. Representative single or composite images are shown in Figure 1.

For the photometry of all data, measurements of 248370 and 10–30 nearby reference stars were performed using IRAF software (Tody 1986, 1993), with absolute calibration performed using field star magnitudes in Sloan bandpasses derived from the `RefCat2` all-sky catalog (which uses the PS1 photometric system; Tonry et al. 2018b). Nucleus or near-nucleus coma photometry of 248370 was performed using circular apertures with sizes chosen using curve-of-growth analyses when the object appeared inactive or circular apertures with fixed radii equivalent to 5000 km at the geocentric distance of the object when it was active. For data in which the object was active, photometry aperture radii, $\theta_{\rm obs}$, were determined from convolving the projected angular equivalent, θ_0, of the desired intrinsic distance (i.e., 5000 km) at the geocentric distance of the comet with the FWHM seeing, θ_s, on a given night using

$$\theta_{\rm obs} = (\theta_0^2 + \theta_s^2)^{1/2}, \tag{1}$$

where $\theta_{\rm obs} \sim 4''$ for most of our observations. Background statistics for comet photometry were measured in nearby regions of blank sky to avoid dust contamination from the object or nearby field stars.

We also measured the surface brightnesses of 248370's dust tail on each night by rotating composite images to make the dust tail horizontal in each image frame, measuring net fluxes in rectangular apertures placed along the length of each tail, and converting those fluxes to surface brightnesses in mag arcsec^{-2} using the measured mean magnitudes of the nucleus for data comprising each composite image for absolute

[24] Written for Python by Maltes Tewes (https://github.com/RyleighFitz/LACosmics).
[25] http://www.cadc-ccda.hia-iha.nrc-cnrc.gc.ca/en/ssois/
[26] https://catch.astro.umd.edu/

Table 1
248370 Activity Observations

UT Date	Telescope	t[a]	Filter	θ_s[b]	ν[c]	r_h[d]	Δ[e]	α[f]	$m(r_h, \Delta, \alpha)$[g]	$m(1, 1, 0)$[h]	A_d/A_n[i]	$Af\rho$[j]	Σ_t[k]
2021 Jul 7	ATLAS	120	Cyan	5.2	16.0	2.391	1.930	24.4	…	…	…	…	…
2021 Jul 9	Palomar	800	g'	2.1	16.6	2.392	1.909	24.2	19.57 ± 0.01	15.14 ± 0.01	2.9 ± 0.5	15.1 ± 0.7	24.24 ± 0.20
2021 Jul 9	FTN	480	g'	1.5	16.6	2.392	1.909	24.2	19.71 ± 0.01	15.28 ± 0.01	2.4 ± 0.5	13.6 ± 0.8	23.87 ± 0.20
2021 Jul 12	Palomar	300	g'	1.4	17.5	2.394	1.877	23.8	19.52 ± 0.02	15.14 ± 0.02	2.9 ± 0.5	16.4 ± 0.8	23.66 ± 0.20
2021 Jul 13	FTN	480	g'	2.4	17.8	2.395	1.867	23.7	19.52 ± 0.02	15.15 ± 0.02	2.9 ± 0.5	14.5 ± 0.8	24.01 ± 0.20
2021 Jul 15	FTN	480	g'	1.5	18.5	2.396	1.842	23.4	19.55 ± 0.02	15.22 ± 0.02	2.6 ± 0.5	14.6 ± 0.8	23.77 ± 0.20
2021 Jul 8	LDT	2400	r'	1.8	16.3	2.391	1.920	24.3	19.14 ± 0.01	14.69 ± 0.01	2.7 ± 0.4	23.2 ± 0.9	23.45 ± 0.20
2021 Jul 9	Palomar	1300	r'	2.1	16.6	2.392	1.909	24.2	19.11 ± 0.01	14.68 ± 0.01	2.8 ± 0.4	22.8 ± 0.8	23.68 ± 0.20
2021 Jul 9	FTN	480	r'	1.4	16.6	2.392	1.909	24.2	19.19 ± 0.01	14.76 ± 0.01	2.5 ± 0.4	22.2 ± 1.0	23.34 ± 0.20
2021 Jul 10	LCOGT 1 m	480	r'	1.8	16.9	2.393	1.898	24.1	19.17 ± 0.02	14.76 ± 0.02	2.5 ± 0.4	21.4 ± 1.0	23.42 ± 0.20
2021 Jul 12	Palomar	900	r'	1.2	17.5	2.394	1.877	23.8	19.12 ± 0.01	14.74 ± 0.01	2.6 ± 0.4	23.2 ± 0.9	23.17 ± 0.20
2021 Jul 13	FTN	480	r'	2.2	17.8	2.395	1.867	23.7	19.05 ± 0.01	14.68 ± 0.01	2.8 ± 0.4	22.6 ± 0.9	23.55 ± 0.20
2021 Jul 14	LCOGT 1 m	1130	r'	2.1	18.1	2.395	1.856	23.6	19.11 ± 0.02	14.76 ± 0.02	2.5 ± 0.4	20.8 ± 1.0	23.66 ± 0.20
2021 Jul 15	LCOGT 1 m	1130	r'	1.7	18.5	2.396	1.842	23.4	19.05 ± 0.01	14.72 ± 0.01	2.6 ± 0.4	22.8 ± 0.9	23.41 ± 0.20
2021 Jul 15	FTN	480	r'	1.4	18.5	2.396	1.842	23.4	19.13 ± 0.01	14.80 ± 0.01	2.4 ± 0.3	21.2 ± 1.0	23.26 ± 0.20
2021 Jul 18	LCOGT 1 m	283	r'	1.7	19.3	2.398	1.815	23.0	19.03 ± 0.06	14.75 ± 0.06	2.5 ± 0.4	22.1 ± 1.9	23.40 ± 0.20
2021 Jul 19	LCOGT 1 m	1130	r'	1.9	19.5	2.399	1.805	22.9	19.06 ± 0.02	14.78 ± 0.02	2.4 ± 0.4	20.7 ± 1.0	23.45 ± 0.20
2021 Jul 21	LCOGT 1 m	1130	r'	2.2	20.1	2.401	1.785	22.5	19.07 ± 0.03	14.83 ± 0.03	2.3 ± 0.3	18.8 ± 1.1	23.75 ± 0.20
2021 Jul 23	LCOGT 1 m	1853	r'	1.9	20.8	2.402	1.762	22.1	19.05 ± 0.03	14.85 ± 0.03	2.2 ± 0.3	19.0 ± 1.1	23.52 ± 0.20
2021 Aug 5	LCOGT 1 m	600	r'	2.1	24.5	2.414	1.648	19.2	18.86 ± 0.02	14.89 ± 0.02	2.1 ± 0.3	17.9 ± 1.0	23.55 ± 0.20
2021 Aug 7	LCOGT 1 m	600	r'	2.0	25.1	2.415	1.632	18.7	18.80 ± 0.01	14.87 ± 0.01	2.2 ± 0.3	18.7 ± 0.9	23.50 ± 0.20
2021 Aug 14	LCOGT 1 m	600	r'	2.0	27.2	2.423	1.577	16.4	18.81 ± 0.01	15.02 ± 0.02	1.8 ± 0.3	15.3 ± 1.0	23.45 ± 0.20
2021 Jul 9	Palomar	900	i'	2.1	16.6	2.392	1.909	24.2	18.98 ± 0.01	14.55 ± 0.01	2.8 ± 0.2	25.7 ± 0.5	23.60 ± 0.20
2021 Jul 9	FTN	480	i'	1.3	16.6	2.392	1.909	24.2	19.16 ± 0.02	14.73 ± 0.02	2.2 ± 0.2	22.2 ± 0.9	23.07 ± 0.20
2021 Jul 12	Palomar	600	i'	1.2	17.5	2.394	1.877	23.8	19.03 ± 0.01	14.65 ± 0.01	2.4 ± 0.2	24.8 ± 0.6	22.94 ± 0.20
2021 Jul 13	FTN	480	i'	2.2	17.8	2.395	1.867	23.7	18.92 ± 0.02	14.55 ± 0.02	2.8 ± 0.2	25.5 ± 0.9	23.40 ± 0.20
2021 Jul 15	FTN	480	i'	1.4	18.5	2.396	1.842	23.4	18.95 ± 0.02	14.62 ± 0.02	2.5 ± 0.2	25.5 ± 0.9	23.07 ± 0.20
2016 Jul 22	Blanco	89	z'	1.1	56.5	2.591	2.571	22.7	20.51 ± 0.10	15.31 ± 0.10	0.7 ± 0.3	7.5 ± 2.4	25.30 ± 0.50
2021 Jul 9	FTN	480	z'	1.2	16.6	2.392	1.909	24.2	19.05 ± 0.04	14.62 ± 0.04	2.2 ± 0.5	24.5 ± 2.1	23.08 ± 0.30
2021 Jul 13	FTN	480	z'	2.1	17.8	2.395	1.867	23.7	18.84 ± 0.03	14.48 ± 0.03	2.6 ± 0.5	27.2 ± 1.9	23.40 ± 0.30
2021 Jul 15	FTN	480	z'	1.3	18.5	2.396	1.842	23.4	18.92 ± 0.03	14.59 ± 0.03	2.2 ± 0.5	25.5 ± 1.9	23.06 ± 0.30

Notes.
[a] Total integration time in seconds.
[b] FWHM seeing in arcseconds.
[c] True anomaly in degrees.
[d] Heliocentric distance in au.
[e] Geocentric distance in au.
[f] Solar phase angle (Sun–object–Earth) in degrees.
[g] Mean apparent coma magnitude (measured using 5000 km radius photometry apertures).
[h] Computed absolute magnitude corresponding to measured apparent magnitude assuming an H, G phase function, where $G = 0.15$.
[i] Inferred ratio of effective scattering cross-sectional areas of coma dust (within 5000 km radius photometry apertures) and the nucleus, where listed uncertainties only reflect photometric measurement uncertainty and not potential nucleus rotational variability.
[j] The $A(\alpha = 0°)f\rho$ values, computed using Equation (4) and 5000 km photometry apertures, in centimeters.
[k] Dust tail surface brightness in mag arcsec^{-2}, as measured in a 1500 km $\times$ 10,000 km rectangular aperture, as described in the text.

Table 2
248370 Nucleus Observations

UT Date	Tel.[a]	N[b]	t[c]	Filter	ν[d]	r_h[e]	Δ[f]	α[g]	$m(r_h, \Delta, \alpha)$[h]	$m(1, 1, 0)$[i]
2010 Aug 6	PS1	1	43	g'	354.7	2.389	1.377	2.0	19.17 ± 0.03	16.35 ± 0.03
2010 Sep 6	PS1	2	86	g'	3.8	2.388	1.463	12.2	20.08 ± 0.05	16.63 ± 0.05
2011 Nov 24	PS1	2	86	g'	109.4	3.150	2.180	4.1	21.20 ± 0.13	16.64 ± 0.13
2011 Dec 1	PS1	2	86	g'	110.6	3.164	2.180	1.4	20.98 ± 0.10	16.60 ± 0.10
Median[j]	…	…	…	g'	…	…	…	…	…	16.62 ± 0.13
2010 Aug 5	PS1	1	40	r'	354.4	2.389	1.378	2.5	18.81 ± 0.03	15.95 ± 0.03
2011 Nov 24	PS1	2	80	r'	109.4	3.150	2.180	4.0	20.74 ± 0.10	16.19 ± 0.10
2018 Dec 15	Blanco	1	45	r'	191.7	3.733	3.508	15.2	22.63 ± 0.31	16.20 ± 0.31
2020 Feb 4	Blanco	2	81	r'	248.9	3.165	3.059	18.1	21.91 ± 0.11	16.04 ± 0.11
Median[j]	…	…	…	r'	…	…	…	…	…	16.12 ± 0.10
2004 Jul 8	CFHT	3	540	i'	287.5	2.740	2.028	17.7	20.72 ± 0.03	16.07 ± 0.03
2010 Aug 2	PS1	1	45	i'	353.5	2.390	1.383	3.9	19.01 ± 0.05	16.05 ± 0.05
2010 Aug 31	PS1	2	90	i'	2.1	2.388	1.429	9.8	19.23 ± 0.04	15.93 ± 0.04
2011 Nov 30	PS1	2	90	i'	110.4	3.162	2.179	1.9	20.26 ± 0.09	15.84 ± 0.09
2015 Aug 18	SkyMapper	1	100	i'	320.3	2.483	1.888	21.8	20.72 ± 0.26	16.31 ± 0.26
Median[j]	…	…	…	i'	…	…	…	…	…	16.05 ± 0.11
2010 Jun 14	PS1	2	60	z'	339.3	2.416	1.728	21.1	20.07 ± 0.13	15.93 ± 0.13
2010 Oct 30	PS1	2	60	z'	19.6	2.413	2.018	23.8	20.48 ± 0.23	15.93 ± 0.13
2020 Feb 10	Blanco	1	199	z'	250.0	3.152	2.960	18.2	21.59 ± 0.14	15.80 ± 0.14
Median[j]	…	…	…	z'	…	…	…	…	…	15.93 ± 0.08

Notes.
[a] Telescope used.
[b] Number of exposures.
[c] Total integration time in seconds.
[d] True anomaly in degrees.
[e] Heliocentric distance in au.
[f] Geocentric distance in au.
[g] Solar phase angle (Sun–object–Earth) in degrees.
[h] Mean apparent magnitude in specified filter.
[i] Computed absolute magnitude corresponding to measured apparent magnitude assuming IAU H, G phase function behavior, where $G = 0.15$.
[j] Median values of computed absolute magnitudes, where standard deviations are used as uncertainties.

Table 3
248370 Colors

UT Date	Telescope	Coma			Tail		
		$g' - r'$	$r' - i'$	$i' - z'$	$g' - r'$	$r' - i'$	$i' - z'$
2021 Jul 9	Palomar	0.47 ± 0.01	0.13 ± 0.01	…	0.56 ± 0.30	0.08 ± 0.30	…
2021 Jul 9	FTN	0.52 ± 0.02	0.03 ± 0.03	0.14 ± 0.04	0.53 ± 0.30	0.27 ± 0.30	-0.02 ± 0.40
2021 Jul 12	Palomar	0.42 ± 0.02	0.08 ± 0.01	…	0.49 ± 0.30	0.23 ± 0.30	…
2021 Jul 13	FTN	0.47 ± 0.02	0.13 ± 0.03	0.05 ± 0.04	0.45 ± 0.30	0.16 ± 0.30	-0.01 ± 0.40
2021 Jul 15	FTN	0.50 ± 0.02	0.10 ± 0.03	0.03 ± 0.04	0.51 ± 0.30	0.19 ± 0.30	0.01 ± 0.40
Median[a]	…	0.47 ± 0.03	0.10 ± 0.04	0.05 ± 0.05	0.51 ± 0.04	0.19 ± 0.07	-0.01 ± 0.01

Note.
[a] Median values of computed colors, where standard deviations are used as uncertainties.

photometric calibration. We chose rectangular apertures that extended 750 km above and below the tail's central axis in the vertical direction (i.e., $\sim 2''$ in total height for most of our observations) and from 5000 to 15,000 km (i.e., from $\sim 4''$ to $\sim 12''$ for most of our observations) from the nucleus in the horizontal direction, where the angular sizes of these apertures were computed in the same manner described earlier for near-nucleus photometry apertures. The details of this method of measuring surface brightnesses were chosen to maximize S/N while also minimizing the nucleus flux contribution by focusing on the bright central core of the tail and measuring close, but not too close, to the nucleus where the tail is brightest.

Photometric results for data obtained when 248370 appeared active and inactive are shown in Tables 1 and 2, respectively. Colors computed by comparing coma magnitudes or tail surface brightnesses in different filters for nights on which multifilter data were obtained are shown in Table 3.

3.2. Nucleus Properties

Using measured apparent magnitudes of 248370 from archival data, we derive magnitudes normalized to $r_h = \Delta = 1$ au and $\alpha = 0°$, or $m(1, 1, 0)$, by assuming inverse-square-law fading and IAU H, G phase function behavior (Bowell et al. 1989), where

$G = 0.15$ (Table 2). We then take the medians of these computed $m(1, 1, 0)$ values to estimate absolute magnitudes in each filter. We estimate 248370's absolute magnitudes to be $H_g = 16.62 \pm 0.13$, $H_r = 16.12 \pm 0.10$, $H_i = 16.05 \pm 0.11$, and $H_z = 15.93 \pm 0.08$ (Table 2), corresponding to nucleus colors of $g' - r' = 0.50 \pm 0.16$, $r' - i' = 0.07 \pm 0.15$, and $i' - z' = 0.12 \pm 0.14$, which, within the uncertainties, are effectively solar (e.g., Holmberg et al. 2006). These colors are consistent with a C-type taxonomic classification (see DeMeo & Carry 2013), which is the most likely classification expected for an outer main-belt asteroid like 248370, but large uncertainties on the colors derived here from sparse archival data mean that other taxonomic types cannot necessarily be excluded at this time. Using $V = g' - 0.565(g' - r') - 0.016$ (Jordi et al. 2006), we find an equivalent V-band absolute magnitude of $H_V = 16.32 \pm 0.10$.

Using

$$r_n = \left(\frac{2.24 \times 10^{22}}{p_V} \times 10^{0.4(m_{\odot,V} - H_V)}\right)^{1/2}, \tag{2}$$

where we use $p_V = 0.054 \pm 0.012$ (Mainzer et al. 2019) for the object's V-band albedo and $m_{\odot,V} = -26.71 \pm 0.03$ for the apparent V-band magnitude of the Sun (Hardorp 1980), we find an effective nucleus radius of $r_n = 1.6 \pm 0.2$ km, or slightly smaller than the radius computed by Mainzer et al. (2019).

The ranges in computed absolute magnitudes in each filter are $\Delta m_g = 0.29$, $\Delta m_r = 0.25$, $\Delta m_i = 0.23$, and $\Delta m_z = 0.13$. These values are not particularly meaningful given the small number of data points used to derive them, but in the present absence of better measurements, they suggest that 248370's photometric range due to rotation is $\Delta m \gtrsim 0.3$ mag, implying a minimum axis ratio of $a/b = 1.3$.

3.3. Activity Properties

3.3.1. Dust Composition

We find mean coma colors of $g' - r' = 0.47 \pm 0.03$, $r' - i' = 0.10 \pm 0.04$, and $i' - z' = 0.05 \pm 0.05$ and mean dust tail colors of $g' - r' = 0.51 \pm 0.04$, $r' - i' = 0.19 \pm 0.07$, and $i' - z' = -0.01 \pm 0.01$ (Table 3). Within the uncertainties, the coma and dust tail colors are comparable to one another, indicating that both are dominated by dust of similar composition with no apparent color gradient with distance from the nucleus that might indicate the presence of a significant near-nucleus gas coma. The apparent compositional similarity of coma and tail dust also means that we see no evidence of grain fragmentation or loss of icy grains to sublimation that could cause overall color changes to the observed dust. The colors of both are also similar within the uncertainties to the colors found for the bare nucleus (Section 3.2), suggesting that the dust coma and tail are compositionally similar to the nucleus's surface regolith.

3.3.2. Activity Strength and Evolution

From our calculations of 248370's absolute magnitudes (Section 3.2), we find that the near-nucleus region of the object was ~0.5 mag brighter than expected for the inactive nucleus on 2016 July 22 and ~1 mag brighter than expected in 2021 (Table 1). We also compute the ratios, A_d/A_n, of the scattering cross sections of ejected near-nucleus dust within our 5000 km photometry apertures and the underlying nucleus when 248370 was active using

$$A_d \Big/ A_n = \frac{1 - 10^{0.4(m(1,1,0)-H)}}{10^{0.4(m(1,1,0)-H)}} \tag{3}$$

(e.g., Hsieh et al. 2021). We find $A_d/A_n = 0.7 \pm 0.3$ on 2016 July 22 and $1.8 < A_d/A_n < 2.9$ in 2021 (Table 1).

Plotting $m(1, 1, 0)$ and A_d/A_n as functions of time, we see that the coma faded during our 2021 observations (Figures 2(a) and (b)), declining in intrinsic brightness by ~0.35 mag (or ~25%) in 37 days. Increasing activity strength would suggest ongoing dust production and therefore the action of a prolonged, possibly sublimation-driven, emission event. However, declining activity strength does not necessarily rule out a sublimation-driven emission event, especially at the relatively gradual rate (~0.01 mag day^{-1}) seen for 248370, similar to the rate of fading of the coma of confirmed recurrently active MBC 259P/Garradd (Hsieh et al. 2021) of ~0.015 mag day^{-1} observed after its discovery in 2008 (Jewitt et al. 2009).

Despite the fading of 248370's coma, the dust tail remained relatively consistent in brightness during our observations (Table 1; Figure 2(c)), suggesting that the tail may consist of larger particles, on average, than the coma. Larger particles in the tail would be dissipated by radiation pressure more slowly than presumably smaller particles in the coma, which would explain the slower fading of the tail to apparently weakening dust production from the nucleus.

For reference, we also compute $A(\alpha = 0°)f\rho$ values (hereafter $Af\rho$), which are nominally independent of photometry aperture sizes for observations of comae with r^{-1} radial profiles and given by

$$A(\alpha = 0°)f\rho = \frac{(2r_h\Delta)^2}{\rho} 10^{0.4[m_\odot - m_d(r_h,\Delta,0)]} \tag{4}$$

(A'Hearn et al. 1984), where r_h is in au, Δ is in centimeters, ρ is the physical radius in centimeters of the photometry aperture at the geocentric distance of the comet, $m_\odot$ is the Sun's apparent magnitude in the specified filter (using $m_{g,\odot} = -26.60$, $m_{r,\odot} = -27.05$, $m_{i,\odot} = -27.17$, and $m_{z,\odot} = -27.21$; Hardorp 1980; Holmberg et al. 2006; Jordi et al. 2006), and $m_d(r_h, \Delta, 0)$ is the phase angle–normalized (to $\alpha = 0°$) magnitude of the excess dust mass of the comet (i.e., with the flux contribution of the nucleus subtracted out). These results are tabulated in Table 1, where we see fading behavior similar to that seen for $m(1, 1, 0)$ and A_d/An.

3.3.3. Dust Ejection Parameter Constraints

Order-of-magnitude constraints on 248370's dust ejection velocities can be obtained by analyzing the sunward extent of the object's coma, as well as the width of its dust tail. On UT 2021 July 12, we measure an HWHM value for the sunward portion of 248370's coma of $\theta_{\rm obs}/2 = 0\farcs68$, while nearby field stars had HWHM values of $\theta_s/2 = 0\farcs61$. Using an analogous form of Equation (1) to compute an intrinsic half-width of the coma, $\theta_0/2$, in the absence of atmospheric seeing, we find $\theta_0/2 = 0\farcs3$, or ~400 km at the geocentric distance of the object. The distance scale on which dust grains ejected sunward with a terminal ejection velocity of v_g are turned back by solar

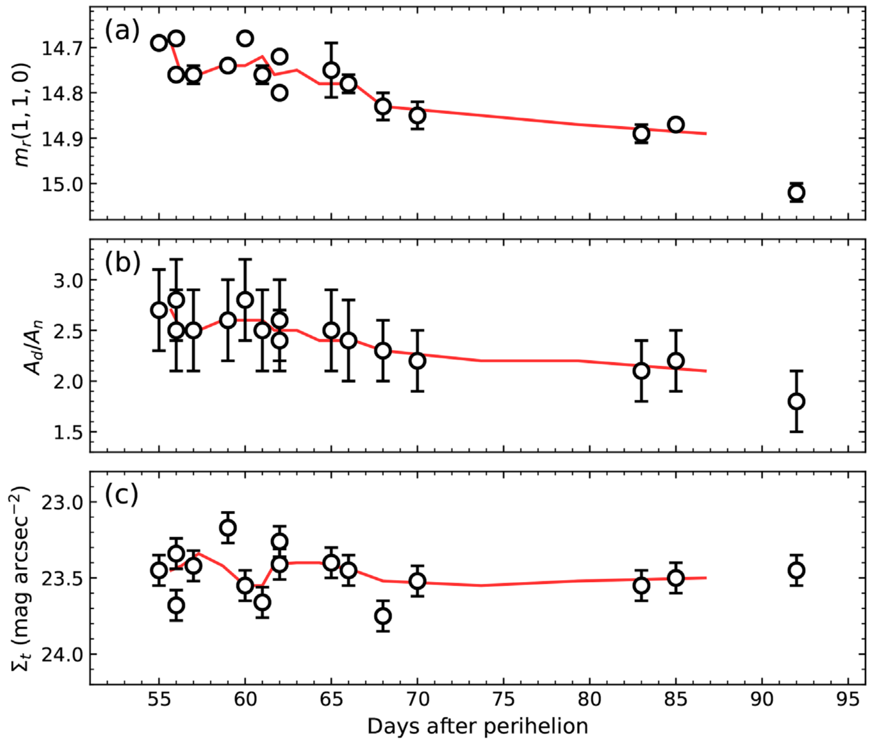

Figure 2. Plots of (a) r'-band near-nucleus magnitudes normalized to $r_h = \Delta = 1$ au and $\alpha = 0°$, (b) inferred ratios of dust-scattering cross sections to nucleus-scattering cross sections measured within 5000 km radius photometry apertures, and (c) surface brightnesses in mag arcsec^{-1} of a fixed portion of the dust tail computed for 248370 from UT 2021 July 8 to 2021 August 14 as a function of days after perihelion (UT 2021 May 14), where red lines in each panel show moving medians (computed for groups of three data points each) for each quantity.

radiation pressure is given by

$$X_R \sim \frac{v_g^2}{2\beta_d g_\odot} \cdot \left(\frac{r_h}{1\ \mathrm{au}}\right)^2 \tag{5}$$

(see Jewitt & Meech 1987), where $g_\odot = 0.006\ \mathrm{m\,s^{-2}}$ is the gravitational acceleration to the Sun at 1 au, β_d is the ratio of the acceleration experienced by a particle due to solar radiation pressure to the local acceleration due to solar gravity (Burns et al. 1979), and $v_g \propto \beta_d^{1/2}$ for dust particles accelerated by outflowing gas, meaning that X_R as computed in Equation (5) is nominally independent of β_d. Comet dust modeling analyses commonly use β_d to represent particle sizes, where $a_d \approx \beta_d^{-1}$ gives the approximate corresponding dust particle radii, a_d, in microns. Using $X_R = 400$ km, Equation (5) gives $v_g \sim 0.9\beta_d^{1/2}$ $\mathrm{m\,s^{-1}}$, or about half the ejection velocities found for 133P/Elst-Pizarro (Jewitt et al. 2014), another MBC very similar in morphology to 248370 and one that has been previously identified to have low dust ejection velocities (e.g., Hsieh et al. 2004).

Meanwhile, measuring the tail in the composite image for UT 2021 July 12 in intervals of 60 pixels ($10\overset{''}{.}5$) along the tail, we find a median FWHM of $\theta_{\mathrm{obs}} = 1\overset{''}{.}6$ over the $90''$ of the tail closest to the nucleus, increasing from $\theta_{\mathrm{obs}} \sim 1\overset{''}{.}5$ at $10''$ from the nucleus to $\theta_{\mathrm{obs}} \sim 1\overset{''}{.}7$ at $90''$ from the nucleus. Low S/N prevents reliable measurements of the tail's width beyond $\sim 90''$, but visually, the tail appears to maintain a similar narrow morphology along its entire visible length, broadening only very gradually with increasing distance from the nucleus. Using Equation (1), we find that $\theta_{\mathrm{obs}} = 1\overset{''}{.}6$ corresponds to an intrinsic median tail FWHM of $\theta_0 = 1\overset{''}{.}0$, or a physical width of $w_T \sim 1400$ km projected in the plane of the sky. At the time of observation, the orbit plane angle of 248370 with respect to Earth was just $0\overset{\circ}{.}03$, so our measured projected width can be considered close to the true width of the tail perpendicular to the object's orbit plane.

Following Jewitt et al. (2014), the component of the terminal dust ejection velocity perpendicular to the orbital plane, V, can be computed using

$$V = a_d^{-1/2} \cdot \left(\frac{g_\odot}{r_h[\mathrm{au}]^2} \cdot \frac{w_T^2}{8\ell_T}\right)^{1/2}, \tag{6}$$

where ℓ_T is the distance from the nucleus at which w_T is measured, and a_d is in microns. Using $w_T \sim 1400$ km and a reference distance from the nucleus of $50''$ ($\ell_T \sim 6.8 \times 10^4$ km), we obtain $V = 1.9 a_d^{-1/2}\ \mathrm{m\,s^{-1}}$, similar to the result derived for 133P by Jewitt et al. (2014). From these analyses of both the coma and tail of 248370, we thus conclude that its activity is characterized by extremely small terminal dust ejection velocities on the order of $\sim 1\ \mathrm{m\,s^{-1}}$ for micron-sized particles and $\sim 5\ \mathrm{cm\,s^{-1}}$ for millimeter-sized particles. Asteroid 248370 has an estimated escape velocity of $v_{\mathrm{esc}} = 1.4\ \mathrm{m\,s^{-1}}$, assuming it is a spherical body with a radius of $r_n = 1.6$ km and bulk density of $\rho_n = 1400\ \mathrm{kg\,m^{-3}}$ (i.e., consistent with C-type asteroids; Britt et al. 2002), which may set a limit on the size of the particles that are able to escape its gravity (where we note, however, that the terminal velocities calculated above apply to particles that have already escaped from the object's gravitational influence). That said, rapid rotation, nucleus elongation, or both could act to reduce or negate the effective gravity felt by dust particles at certain locations on the nucleus surface, allowing even extremely large particles to be ejected, similar to what may be occurring on 133P (Jewitt et al. 2014).

Performing a simple (zero-ejection velocity) dust modeling analysis using the online Comet Toolbox,[27] we find that particles with $\beta = 1$ would take ∼20 days to reach an apparent angular separation from the nucleus of $\sim 9'$ (the visible length of the tail on UT 2021 July 12; Figure 1(f)). Meanwhile, particles with $\beta = 0.1$, 0.01, and 0.001 (or $a \sim 10$ μm, 100 μm, and 1 mm), which span the range of particle sizes found for other MBCs (e.g., Hsieh et al. 2009; Licandro et al. 2013; Jewitt et al. 2014), would take 60, 150, and 430 days, respectively, to reach the same apparent separation. Without additional particle size constraints at the present time, however, we cannot meaningfully constrain the likely ejection times of the most distant dust grains in 248370's tail. We note that if activity began when 248370 was at $\nu = 300°$ (the earliest activation point confirmed to date for an MBC; Hsieh & Sheppard 2015), which the object passed on 2020 October 22, particles as large as $a \sim 400$ μm ($\beta = 0.0025$) would have been able to reach a $9'$ separation from the nucleus by 2021 July 12.

3.4. Future Work

The discovery that 248370 is recurrently active near perihelion strongly suggests that sublimation is a primary driver of its activity, although it does not rule out other processes that could also contribute to the current observed activity. In particular, we suggest in Section 3.3.3 that rapid rotation and nucleus elongation could potentially play a significant role in the dust ejection process, especially for larger particles. As such, measurement of 248370's rotational period and nucleus shape, as well as its taxonomic type, should be considered a high priority once its current activity ends. Continued monitoring of 248370's current activity is also highly encouraged to enable further characterization of the object's fading behavior, which can help constrain the dust grain size distribution.

A detailed dynamical analysis of 248370 is outside the scope of this paper but should also be performed in the near future. Issues to consider include whether the object can be linked to any dynamical asteroid families (e.g., Hsieh et al. 2018), its long-term dynamical stability and whether it may be an implanted object (e.g., Hsieh & Haghighipour 2016), and whether it follows the dynamical trends found for previously discovered MBCs (Kim et al. 2018).

In the long term, 248370 will be well placed for monitoring during the approach to its next perihelion passage on UT 2026 September 3. It becomes observable from the Southern Hemisphere in 2026 February at $\nu \sim 300°$, i.e., the earliest activation point confirmed to date for an MBC, as discussed earlier. Monitoring during this time will be extremely valuable for further confirming the recurrent nature of 248370's activity, constraining the orbital range over which activity occurs (with implications for constraining ice depth on the object, as well as its active lifetime), measuring initial dust production rates, and comparing the object's activity levels from one orbit to another, as well as to other MBCs.

H.H.H., C.O.C., M.S.P.K., M.M.K., J.P., S.S.S., A.T., and C.A.T. acknowledge support from the NASA Solar System Observations program (grant 80NSSC19K0869). C.O.C. is also supported by the National Science Foundation Graduate Research Fellowship Program under grant No. (2018258765). Any opinions, findings, and conclusions or recommendations expressed in this material are those of the author(s) and do not necessarily reflect the views of the National Science Foundation. The work of J.P. was conducted at the Jet Propulsion Laboratory, California Institute of Technology, under a contract with the National Aeronautics and Space Administration (80NM0018D0004). H.U., T.A., R.M., P.R., and B.W. were supported by a UK Science and Technology Facilities Council (STFC) "Spark Award" grant for the Comet Chasers school outreach program.

We are grateful to K. Peffer, P. Nied, C. Heffner, and T. Barlow for assistance in obtaining observations with Palomar; I. Nisley and C. Siqueiros for assistance in obtaining observations with LDT; and an anonymous referee for helpful comments that improved this manuscript. This research made use of `astropy`, a community-developed core `python` package for astronomy; `uncertainties` (version 3.0.2), a `python` package for calculations with uncertainties by E. O. Lebigot; scientific software at http://www.comet-toolbox.com (Vincent 2014); and NASA's Astrophysics Data System Bibliographic Services.

This research made use of data obtained at the Lowell Discovery Telescope (LDT). Lowell Observatory is a private, nonprofit institution dedicated to astrophysical research and public appreciation of astronomy and operates the LDT in partnership with Boston University, the University of Maryland, the University of Toledo, Northern Arizona University, and Yale University. Partial support of the LDT was provided by Discovery Communications. LMI was built by Lowell Observatory using funds from the National Science Foundation (NSF grant AST-1005313; PI: P. Massey). This work also used observations obtained at the Hale Telescope at Palomar Observatory, which is operated as part of a continuing collaboration between the California Institute of Technology, NASA/JPL, Oxford University, Yale University, and the National Astronomical Observatories of China.

This work also includes observations from the Las Cumbres Observatory global telescope network. Specifically, this paper uses observations made with the MuSCAT3 instrument, developed by the Astrobiology Center and with financial support from JSPS KAKENHI (JP18H05439) and JST PRESTO (JPMJPR1775), at Faulkes Telescope North on Maui, Hawaii, operated by the Las Cumbres Observatory.

Observations with the LCOGT 1 m were obtained as part of the LCOGT Outbursting Objects Key (LOOK) Project (KEY2020B-009), while FTN observations were obtained via the aforementioned Comet Chasers school outreach program. The Comet Chasers program is part of the Faulkes Telescope Project (FTPEPO2014A-004), which is partly funded by the Dill Faulkes Educational Trust. Pupils from three schools in Wales (St Mary's Catholic Primary School Bridgend, Mount Street Junior School Brecon, and Ynysowen Community Primary School) made observations.

The Asteroid Terrestrial-impact Last Alert System (ATLAS) project is primarily funded to search for near-Earth asteroids through NASA grants NN12AR55G, 80NSSC18K0284, and 80NSSC18K1575. The ATLAS science products have been made possible through the contributions of the University of Hawaii Institute for Astronomy, Queens University Belfast, the Space Telescope Science Institute, the South African

[27] http://comet-toolbox.com/FP.html

Astronomical Observatory, and the Millennium Institute of Astrophysics (MAS), Chile.

This research used the facilities of the Canadian Astronomy Data Centre operated by the National Research Council of Canada with the support of the Canadian Space Agency. The Pan-STARRS1 surveys (PS1) and the PS1 public science archive have been made possible through contributions by the Institute for Astronomy, the University of Hawaii, the Pan-STARRS Project Office, the Max Planck Society and its participating institutes, the Max Planck Institute for Astronomy, Heidelberg and the Max Planck Institute for Extraterrestrial Physics, Garching, The Johns Hopkins University, Durham University, the University of Edinburgh, Queen's University Belfast, the Harvard-Smithsonian Center for Astrophysics, the Las Cumbres Observatory Global Telescope Network Inc., the National Central University of Taiwan, the Space Telescope Science Institute, the National Aeronautics and Space Administration (NASA) under grant NNX08AR22G, the National Science Foundation (NSF) under grant AST-1238877, the University of Maryland, Eotvos Lorand University (ELTE), the Los Alamos National Laboratory, and the Gordon and Betty Moore Foundation.

This project used data obtained with the Dark Energy Camera (DECam), which was constructed by the Dark Energy Survey (DES) collaborating institutions: Argonne National Lab, the University of California Santa Cruz, the University of Cambridge, Centro de Investigaciones Energeticas, Medioambientales y Tecnologicas-Madrid, the University of Chicago, University College London, the DES-Brazil consortium, the University of Edinburgh, ETH-Zurich, the University of Illinois at Urbana-Champaign, Institut de Ciencies de l'Espai, Institut de Fisica d'Altes Energies, Lawrence Berkeley National Lab, Ludwig-Maximilians Universitat, the University of Michigan, the National Optical Astronomy Observatory, the University of Nottingham, Ohio State University, the University of Pennsylvania, the University of Portsmouth, SLAC National Lab, Stanford University, the University of Sussex, and Texas A&M University. Funding for DES, including DECam, has been provided by the U.S. Department of Energy, National Science Foundation, Ministry of Education and Science (Spain), Science and Technology Facilities Council (UK), Higher Education Funding Council (England), National Center for Supercomputing Applications, Kavli Institute for Cosmological Physics, Financiadora de Estudos e Projetos, Fundação Carlos Chagas Filho de Amparo a Pesquisa, Conselho Nacional de Desenvolvimento Científico e Tecnológico and the Ministério da Ciência e Tecnologia (Brazil), the German Research Foundation–sponsored cluster of excellence "Origin and Structure of the Universe," and the DES collaborating institutions.

The national facility capability for SkyMapper has been funded through ARC LIEF grant LE130100104 from the Australian Research Council, awarded to the University of Sydney, the Australian National University, Swinburne University of Technology, the University of Queensland, the University of Western Australia, the University of Melbourne, Curtin University of Technology, Monash University, and the Australian Astronomical Observatory. SkyMapper is owned and operated by the Australian National University's Research School of Astronomy and Astrophysics. The survey data were processed and provided by the SkyMapper Team at ANU. The SkyMapper node of the All-Sky Virtual Observatory (ASVO) is hosted at the National Computational Infrastructure (NCI). Development and support of the SkyMapper node of the ASVO has been funded in part by Astronomy Australia Limited (AAL) and the Australian Government through the Commonwealth's Education Investment Fund (EIF) and National Collaborative Research Infrastructure Strategy (NCRIS), particularly the National eResearch Collaboration Tools and Resources (NeCTAR) and the Australian National Data Service Projects (ANDS).

Finally, this work made use of observations obtained with MegaPrime/MegaCam, a joint project of CFHT and CEA/DAPNIA, at the Canada–France–Hawaii Telescope (CFHT), which is operated by the National Research Council (NRC) of Canada, the Institut National des Science de l'Univers of the Centre National de la Recherche Scientifique (CNRS) of France, and the University of Hawaii. The observations at the Canada–France–Hawaii Telescope were performed with care and respect from the summit of Maunakea, which is a significant cultural and historic site.

Facilities: Blanco (DECam), CFHT (MegaCam), PS1, LDT (LMI), Hale (WASP), LCOGT, FTN (MuSCAT3), Skymapper.

Software: `astropy` (Astropy Collaboration et al. 2018), `astroquery` (Ginsburg et al. 2019), `IRAF` (Tody 1986, 1993), `L.A.Cosmic` (van Dokkum 2001; van Dokkum et al. 2012), `uncertainties` (v3.0.2; E. O. Lebigot), `RefCat2` (Tonry et al. 2018b), Comet Toolbox (Vincent 2014).

ORCID iDs

Henry H. Hsieh https://orcid.org/0000-0001-7225-9271
Colin O. Chandler https://orcid.org/0000-0001-7335-1715
Larry Denneau https://orcid.org/0000-0002-7034-148X
Alan Fitzsimmons https://orcid.org/0000-0003-0250-9911
Nicolas Erasmus https://orcid.org/0000-0002-9986-3898
Michael S. P. Kelley https://orcid.org/0000-0002-6702-7676
Matthew M. Knight https://orcid.org/0000-0003-2781-6897
Tim A. Lister https://orcid.org/0000-0002-3818-7769
Jana Pittichová https://orcid.org/0000-0002-5736-1857
Scott S. Sheppard https://orcid.org/0000-0003-3145-8682
Audrey Thirouin https://orcid.org/0000-0002-1506-4248
Chadwick A. Trujillo https://orcid.org/0000-0001-9859-0894
Helen Usher https://orcid.org/0000-0002-8658-5534
Edward Gomez https://orcid.org/0000-0001-5749-1507
Joey Chatelain https://orcid.org/0000-0002-1278-5998
Sarah Greenstreet https://orcid.org/0000-0002-4439-1539
Tony Angel https://orcid.org/0000-0003-4881-6255
Richard Miles https://orcid.org/0000-0002-0442-4885
Ben Wooding https://orcid.org/0000-0003-4227-0415

References

A'Hearn, M. F., Schleicher, D. G., Millis, R. L., Feldman, P. D., & Thompson, D. T. 1984, AJ, 89, 579
Astropy Collaboration, Price-Whelan, A. M., Sipőcz, B. M., et al. 2018, AJ, 156, 123
Bida, T. A., Dunham, E. W., Massey, P., & Roe, H. G. 2014, Proc. SPIE, 9147, 91472N
Boulade, O., Charlot, X., Abbon, P., et al. 2003, Proc. SPIE, 4841, 72
Bowell, E., Hapke, B., Domingue, D., et al. 1989, in Asteroids II (Tucson, ARI: Univ. of Arizona Press), 524
Britt, D. T., Yeomans, D., Housen, K., & Consolmagno, G. 2002, in Asteroids III (Tucson, ARI: Univ. of Arizona Press), 485
Brown, T. M., Baliber, N., Bianco, F. B., et al. 2013, PASP, 125, 1031

Burns, J. A., Lamy, P. L., & Soter, S. 1979, Icar, 40, 1
Chambers, K. C., Magnier, E. A., Metcalfe, N., et al. 2016, arXiv:1612.05560
Chandler, C. O., Trujillo, C. A., & Hsieh, H. H. 2021a, CBET, 5005, 1
Chandler, C. O., Trujillo, C. A., & Hsieh, H. H. 2021b, ApJL, 922, L8
DeMeo, F. E., & Carry, B. 2013, Icar, 226, 723
Fitzsimmons, A., Erasmus, N., Thirouin, A., Hsieh, H. H., & Green, D. W. E. 2021, CBET, 4995, 1
Flaugher, B., Diehl, H. T., Honscheid, K., et al. 2015, AJ, 150, 150
Flewelling, H. A., Magnier, E. A., Chambers, K. C., et al. 2020, ApJS, 251, 7
Ginsburg, A., Sipőcz, B. M., Brasseur, C. E., et al. 2019, AJ, 157, 98
Gwyn, S. D. J., Hill, N., & Kavelaars, J. J. 2012, PASP, 124, 579
Hardorp, J. 1980, A&A, 91, 221
Holmberg, J., Flynn, C., & Portinari, L. 2006, MNRAS, 367, 449
Hsieh, H. H., & Haghighipour, N. 2016, Icar, 277, 19
Hsieh, H. H., Ishiguro, M., Knight, M. M., et al. 2021, PSJ, 2, 62
Hsieh, H. H., & Jewitt, D. 2006, Sci, 312, 561
Hsieh, H. H., Jewitt, D., & Ishiguro, M. 2009, AJ, 137, 157
Hsieh, H. H., Jewitt, D. C., & Fernández, Y. R. 2004, AJ, 127, 2997
Hsieh, H. H., Novaković, B., Kim, Y., & Brasser, R. 2018, AJ, 155, 96
Hsieh, H. H., & Sheppard, S. S. 2015, MNRAS, 454, L81
Hsieh, H. H., Yang, B., & Haghighipour, N. 2012, ApJ, 744, 9
Jewitt, D., Hsieh, H., & Agarwal, J. 2015, Asteroids IV (Tucson, ARI: Univ. of Arizona Press), 221
Jewitt, D., Ishiguro, M., Weaver, H., et al. 2014, AJ, 147, 117
Jewitt, D., Yang, B., & Haghighipour, N. 2009, AJ, 137, 4313
Jewitt, D. C., & Meech, K. J. 1987, ApJ, 317, 992
Jordi, K., Grebel, E. K., & Ammon, K. 2006, A&A, 460, 339
Kelley, M. S. P., Bolin, B. T., Buzzi, L., et al. 2021, CBET, 4998, 1
Kim, Y., JeongAhn, Y., & Hsieh, H. H. 2018, AJ, 155, 142
Levine, S. E., Bida, T. A., Chylek, T., et al. 2012, Proc. SPIE, 8444, 844419
Licandro, J., Moreno, F., de León, J., et al. 2013, A&A, 550, A17
Mainzer, A. K., Bauer, J. M., Cutri, R. M., et al. 2019, NASA Planetary Data System; NEOWISE Diameters and Albedos V2.0
McCully, C., Volgenau, N. H., Harbeck, D.-R., et al. 2018, Proc. SPIE, 10707, 107070K
Narita, N., Fukui, A., Yamamuro, T., et al. 2020, Proc. SPIE, 11447, 114475K
Nikzad, S., Jewell, A. D., Hoenk, M. E., et al. 2017, JATIS, 3, 036002
Tody, D. 1986, Proc. SPIE, 627, 733
Tody, D. 1993, in ASP Conf. Ser., 52, Astronomical Data Analysis Software and Systems II (San Francisco, CA: ASP), 173
Tonry, J. L., Stubbs, C. W., Lykke, K. R., et al. 2012, ApJ, 750, 99
Tonry, J. L., Denneau, L., Heinze, A. N., et al. 2018a, PASP, 130, 064505
Tonry, J. L., Denneau, L., Flewelling, H., et al. 2018b, ApJ, 867, 105
van Dokkum, P. G. 2001, PASP, 113, 1420
van Dokkum, P. G., Bloom, J., & Tewes, M. 2012, L.A. Cosmic: Laplacian Cosmic Ray Identification, Astrophysics Source Code Library, ascl:1207.005
Vincent, J. 2014, Asteroids, Comets, Meteors 2014; Comet-toolbox: Numerical simulations of cometary dust tails in your browser, 30 ed. K. Muinonen et al., 565
Wolf, C., Onken, C. A., Luvaul, L. C., et al. 2018, PASA, 35, e010